

Haar Nuclear Norms with Applications to Remote Sensing Imagery Restoration

Shuang Xu¹, Chang Yu², Jiangjun Peng¹, Xiangyong Cao³

¹School of Mathematics and Statistics, Northwestern Polytechnical University, Xi'an, 710021, Shaanxi, China.

²School of Mathematics and Statistics, Xi'an Jiaotong University, Xi'an, 710049, Shaanxi, China.

³School of Electronic and Information Engineering, Xi'an Jiaotong University, Xi'an, 710049, Shaanxi, China.

Abstract

Remote sensing image restoration aims to reconstruct missing or corrupted areas within images. To date, low-rank based models have garnered significant interest in this field. This paper proposes a novel low-rank regularization term, named the Haar nuclear norm (HNN), for efficient and effective remote sensing image restoration. It leverages the low-rank properties of wavelet coefficients derived from the 2-D frontal slice-wise Haar discrete wavelet transform, effectively modeling the low-rank prior for separated coarse-grained structure and fine-grained textures in the image. Experimental evaluations conducted on hyperspectral image inpainting, multi-temporal image cloud removal, and hyperspectral image denoising have revealed the HNN's potential. Typically, HNN achieves a performance improvement of 1-4 dB and a speedup of 10-28x compared to some state-of-the-art methods (e.g., tensor correlated total variation, and fully-connected tensor network) for inpainting tasks.

Keywords: Nuclear norm, tensor nuclear norm, tensor completion, hyperspectral image denoising, remote sensing image cloud removal.

1 Introduction

Remote sensing imagery restoration aims to reconstruct missing or corrupted areas of images [12], including hyperspectral images (HSIs) and multi-temporal images (MTIs), typically represented as multi-dimensional arrays. Inpainting and denoising are key tasks in this restoration process [28, 39]. The mathematical formulations for these tasks are as follows:

$$\min_{\mathcal{X}} R(\mathcal{X}) \quad \text{s. t.} \quad \mathcal{P}_{\Omega}(\mathcal{M}) = \mathcal{P}_{\Omega}(\mathcal{X}), \quad (1)$$

and

$$\min_{\mathcal{X}} R(\mathcal{X}) \quad \text{s. t.} \quad \mathcal{M} = \mathcal{X} + \mathcal{E}, \quad (2)$$

Here \mathcal{E} represents noise, \mathcal{M} is the corrupted image, and \mathcal{X} is the recovered one. Here, Ω indicates the set of indices for observable pixels, $\mathcal{P}_{\Omega}(\cdot)$ is the orthogonal projection onto the observable pixels, and $R(\cdot)$ is the regularization term applied to the recovered images to ensure desired properties such as smoothness or low-rankness.

This problem is typically addressed by low-rank (LR) models, which exploits the intrinsic structure and correlations in the data, under the assumption that data lie in a low-dimensional subspace [50, 30]. These images tend to exhibit spatial and channel redundancies, making LR models particularly effective. The nuclear norm (NN) and its variants, such as the tensor nuclear norm (TNN) [19, 20], are commonly used as LR regularization. TNN, for instance, is extensively applied in various tensor processing problems and is defined as the sum of singular values from the first frontal slice of the singular value tensor, derived from tensor singular value decomposition (TSVD) [14]. Moreover, adjacent pixels in images often have similar values, leading to gradient sparsity. This property gives rise to a new optimization problem:

$$\min_{\mathcal{X}} R(\mathcal{X}) + \lambda \|\nabla \mathcal{X}\|_1, \quad \text{s. t.} \quad \mathcal{P}_{\Omega}(\mathcal{M}) = \mathcal{P}_{\Omega}(\mathcal{X}), \quad (3)$$

where $\|\nabla \mathcal{X}\|_1$ represents the anisotropic total variation (TV) [10], which is the ℓ_1 norm of the

gradient map $\nabla\mathcal{X}$, and $\lambda > 0$ is the tuning parameter that balances the regularization terms. TV improves image restoration but is sensitive to the λ parameter selection, limiting its practicality.

The recently proposed correlated TV (CTV) [24] and tensor CTV (TCTV) [31] address this issue by imposing NN and TNN on the gradient map. For instance, TCTV, defined as the sum of TNNs of gradients along each mode, inherits the LR property from the original tensor and promotes gradient sparsity. In essence, TCTV simultaneously encourages LR and smoothness priors without parameter tuning. Most significantly, minimizing TCTV can achieve exact data recovery with high probability. In contrast to NN and TNN, which models LR prior in the image domain where low- and high-frequencies are entangled, the efficacy of CTV and TCTV stems from its ability to model the high-frequency LR prior, specifically the low-rankness of gradient maps.

However, TCTV and CTV face certain challenges. Firstly, its computation is time-consuming, particularly for high-order images with a significantly larger number of channels than RGB images. For instance, processing an HSI of size $256 \times 256 \times 193$ can take TCTV approximately 2000 seconds, which is 10 times longer than the processing time for TNN. Secondly, while TCTV and CTV effectively models the high-frequency LR prior, neglecting the low-frequency information may result in the loss of crucial data and the color/spectral distortion. This study aims to address these critical issues, and its main contributions are outlined as follows:

(1) Drawing inspiration from the Haar wavelet transform (HWT), we propose a two-dimensional frontal HWT tailored for high-order images to disentangle low- and high-frequencies. Furthermore, we introduce a novel regularizer, the Haar nuclear norm (HNN), which models the LR property for both disentangled low- and high-frequency information, thereby combining LR and smoothness priors at a reduced scale.

(2) The paper establishes the theory of exact recovery for HNN-regularized inpainting and denoising models, providing theoretical guarantees for the effectiveness of the proposed method.

(3) The paper develops an algorithm based on the Alternating Direction Method of Multipliers (ADMM) for solving the HNN-based restoration models. This algorithm ensures efficient computation, making HNN practical for real-world applications. For example, in inpainting experiments, HNN achieves a 1-4dB improvement in performance over state-of-the-art methods with a speedup of 10-28x.

2 Related work

2.1 Low-rank models

Low-rank models can be broadly classified into two categories: matrix/tensor decompositions and low-rank regularization techniques.

2.1.1 Low-rank decomposition models

Matrix decompositions, with SVD as a prime example, are fundamental in low-rank models. SVD represents a matrix as a product of three matrices, enabling it to be expressed as a sum of rank-one matrices, which is key to many low-rank methods. For high-order images, tensor decompositions extend this concept, providing a more suitable framework to capture complex data relationships.

The Canonical Polyadic (CP) decomposition [11] factorizes a tensor into a sum of rank-one tensors, similar to how SVD works for matrices. The Tucker decomposition [29] offers a more flexible representation by expressing a tensor as a core tensor multiplied by factor matrices along each mode, capturing varying correlations. Tensor Train (TT) [21, 15] and Tensor Ring (TR) [40, 18] decompositions represent tensors as chains or rings of third-order tensors, effectively completing images. The recently proposed Fully Connected Tensor Network (FCTN) [48, 49, 41] decomposes a tensor into a sequence of small tensors of the same order, with these tensors interacting to model the relationships between every pair of modes. FCTN holds promise for superior reconstruction of missing pixels [42, 43] but may require careful rank selection. Recently, an architecture searching strategy has enhanced FCTN's data adaptability [49]. Besides exploring advanced decomposition models, the noise modeling techniques, such as non-independent and identically distributed (non-i.i.d.) [3, 34] or asymmetric [35, 13] noise models, have shown promising results for hyperspectral image processing.

2.1.2 Low-rank regularizations

LR regularization encourages solutions with a low-rank structure. For matrices, the NN, the sum of singular values, is a convex relaxation of rank and is used in matrices. Nonetheless, the application of LR regularization to tensors remains an unresolved issue. The Sum of Nuclear Norm (SNN) [17] is the sum of the nuclear norms of all possible matrix representations (matricizations) of a tensor, aiming for low ranks in all two-dimensional unfoldings, thus implicitly encouraging a low-rank structure for the entire tensor. Building upon the recently proposed tensor-tensor product, the TNN [19, 20] is derived and demonstrated to be the convex envelope of the tensor average rank within the unit ball of the tensor spectral norm. In contrast to SNN, TNN provides theoretical guarantees of recovery. Recently,

some more advanced norms for tensors are developed for denoising and inpainting [46, 45], such as the non-convex [6, 22, 5] and non-local [4, 37, 36] variants.

2.2 Low-rank models combined with smoothness

In addition to the LR prior, integrating local smoothness priors or regularizations [44, 32] can greatly improve image reconstruction. Models such as TV-regularized SNN (SNNTV) [16], TV-regularized TNN (TNNTV) [27], and Smooth PARAFAC Completion with TV (SPCTV) [38] are commonly used. However, these methods are sensitive to the TV weight, often requiring extensive parameter tuning [25]. CTV and TCTV address this by modeling LR priors in the gradient domain, promoting both LR and smooth recovery in a regularization. However, TCTV is computationally intensive, taking over 50 minutes for a $512 \times 512 \times 63$ image. Furthermore, CTV and TCTV focus on high-frequency LR information, potentially overlooking important LR details in the image domain.

3 Preliminaries

3.1 Tensor operations

The Frobenius norm of a tensor $\mathcal{A} \in \mathbb{R}^{I_1 \times \dots \times I_N}$ is defined as $\|\mathcal{A}\|_F = \sqrt{\sum_{i_1, \dots, i_N} |a_{i_1 \dots i_N}|^2}$. The mode- n unfolding of a tensor results in a matrix representation, denoted by $\mathbf{A}_{(n)} \in \mathbb{R}^{I_n \times \prod_{i \neq n} I_i}$. The mode- n product of a tensor $\mathcal{A} \in \mathbb{R}^{I_1 \times \dots \times I_N}$ and a matrix $\mathbf{B} \in \mathbb{R}^{J \times I_n}$ results in a new tensor $\mathcal{C} = \mathcal{A} \times_n \mathbf{B} \in \mathbb{R}^{I_1 \times \dots \times I_{n-1} \times J \times I_{n+1} \times \dots \times I_N}$, given by

$$c_{i_1, \dots, i_{n-1}, j, i_{n+1}, \dots, i_N} = \sum_{i_k=1}^{I_k} a_{i_1, \dots, i_{n-1}, i_n, i_{n+1}, \dots, i_N} b_{j i_n}. \quad (4)$$

This can be represented in matrix form as $\mathbf{C}_{(n)} = \mathbf{B} \mathbf{A}_{(n)}$.

Definition 1 (n -Rank [7]). *The n -rank of a tensor \mathcal{A} is the rank of the tensor \mathcal{A} unfolded along mode n , given by $\text{rank}_n(\mathcal{A}) = \text{rank}(\mathbf{A}_{(n)})$.*

Definition 2 (Tucker-Rank [8]). *The Tucker-rank is a tuple of n -ranks, $\text{rank}_T(\mathcal{A}) = (\text{rank}_1(\mathcal{A}), \dots, \text{rank}_N(\mathcal{A}))$.*

3.2 Haar wavelet transform

Definition 3 (1-D Haar Discrete Wavelet Transform). *The 1-D Haar discrete wavelet transform (HWT) of a vector $\mathbf{a} \in \mathbb{R}^N$ is defined by*

$$\mathbf{b} = f(\mathbf{a}) = \mathbf{W}_N \mathbf{a}, \quad (5)$$

where the N -order orthogonal projection matrix \mathbf{W}_N is composed of an $\frac{N}{2} \times N$ block $\mathbf{H}_{N/2}$ and

an $\frac{N}{2} \times N$ block $\mathbf{G}_{N/2}$, and the 1-D inverse HWT (IHWT) is given by

$$\mathbf{a} = f^{-1}(\mathbf{b}) = \mathbf{W}_N^{-1} \mathbf{b} = \mathbf{W}_N^T \mathbf{b}. \quad (6)$$

$\mathbf{H}_{N/2}$ and $\mathbf{G}_{N/2}$ are generally deemed as the average filter and discrete gradient operator, respectively; and \mathbf{W}_N is defined by

$$\mathbf{W}_N = \begin{bmatrix} \mathbf{H}_{N/2} \\ \mathbf{G}_{N/2} \end{bmatrix} = \underbrace{\begin{bmatrix} \frac{\sqrt{2}}{2} & \frac{\sqrt{2}}{2} & 0 & 0 & \dots & 0 & 0 \\ 0 & 0 & \frac{\sqrt{2}}{2} & \frac{\sqrt{2}}{2} & \dots & 0 & 0 \\ \vdots & & & & \ddots & & \vdots \\ 0 & 0 & 0 & 0 & \dots & \frac{\sqrt{2}}{2} & -\frac{\sqrt{2}}{2} \\ \frac{\sqrt{2}}{2} & -\frac{\sqrt{2}}{2} & 0 & 0 & \dots & 0 & 0 \\ 0 & 0 & \frac{\sqrt{2}}{2} & -\frac{\sqrt{2}}{2} & \dots & 0 & 0 \\ \vdots & & & & \ddots & & \vdots \\ 0 & 0 & 0 & 0 & \dots & \frac{\sqrt{2}}{2} & -\frac{\sqrt{2}}{2} \end{bmatrix}}_N, \quad (7)$$

Definition 4 (2-D Haar Discrete Wavelet Transform). *The 2-D Haar discrete wavelet transform (2-D HWT) for a matrix $\mathbf{A} \in \mathbb{R}^{M \times N}$ is defined as*

$$\mathbf{B} = F(\mathbf{A}) = \mathbf{W}_M \mathbf{A} \mathbf{W}_N^T, \quad (8)$$

where \mathbf{W}_M and \mathbf{W}_N are the M -order and N -order projection matrices, respectively. The 2-D inverse HWT (2-D IHWT) is given by

$$\mathbf{A} = F^{-1}(\mathbf{B}) = \mathbf{W}_M^T \mathbf{B} \mathbf{W}_N. \quad (9)$$

2-D HWT processes a matrix $\mathbf{A} \in \mathbb{R}^{M \times N}$ by applying the 1-D HWT to its row vectors and column vectors separately. Consequently, as depicted in Eq. (7), \mathbf{B} can be represented as a block matrix:

$$\begin{aligned} \mathbf{B} &= \mathbf{W}_M \mathbf{A} \mathbf{W}_N^T \\ &= \begin{bmatrix} \mathbf{H}_{M/2} \\ \mathbf{G}_{M/2} \end{bmatrix} \mathbf{A} \begin{bmatrix} \mathbf{H}_{N/2} \\ \mathbf{G}_{N/2} \end{bmatrix}^T \\ &= \begin{bmatrix} \mathbf{H}_{M/2} \mathbf{A} \mathbf{H}_{N/2}^T & \mathbf{H}_{M/2} \mathbf{A} \mathbf{G}_{N/2}^T \\ \mathbf{G}_{M/2} \mathbf{A} \mathbf{H}_{N/2}^T & \mathbf{G}_{M/2} \mathbf{A} \mathbf{G}_{N/2}^T \end{bmatrix} \\ &\triangleq \begin{bmatrix} \mathbf{F}_1(\mathbf{A}) & \mathbf{F}_2(\mathbf{A}) \\ \mathbf{F}_3(\mathbf{A}) & \mathbf{F}_4(\mathbf{A}) \end{bmatrix} \triangleq \begin{bmatrix} \mathbf{B}_1 & \mathbf{B}_2 \\ \mathbf{B}_3 & \mathbf{B}_4 \end{bmatrix}, \end{aligned} \quad (10)$$

where $\mathbf{B}_1, \mathbf{B}_2, \mathbf{B}_3, \mathbf{B}_4$ represent the blocks known as approximation, horizontal, vertical, and diagonal wavelet coefficients, respectively.

The computational complexity of the 2-D HWT, as expressed by $\mathbf{B} = \mathbf{W}_M \mathbf{A} \mathbf{W}_N^T$, is $O(MN(M+N))$, which involves two instances of matrix multiplication. However, \mathbf{W}_M and \mathbf{W}_N are highly sparse matrices with distinctive patterns. The wavelet coefficients can be verified through the following

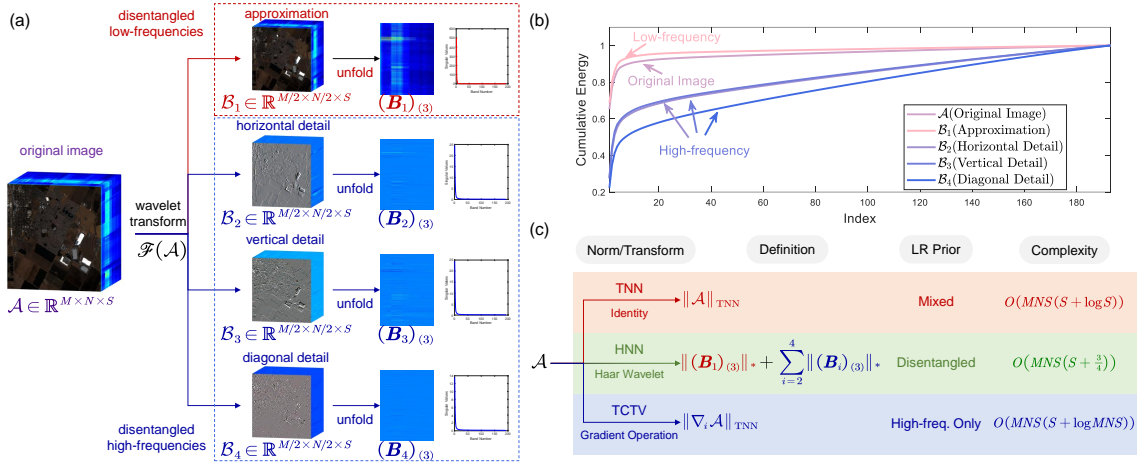


Fig. 1 (a) Typical remote sensing imagery $\mathcal{A} \in \mathbb{R}^{M \times N \times S}$ and its wavelet coefficients, which exhibit rapid decay in singular values. $\mathcal{F}(\cdot)$ represents the 2D FHWT. (b) The CE curves for the original image and wavelet coefficients. (c) Comparison of TNN, TCTV, and HNN, where $\|\cdot\|_*$ denotes the matrix nuclear norm and $\|\cdot\|_{\text{TNN}}$ represents the TNN.

expressions:

$$\begin{aligned}
 \mathcal{B}_1(i, j) &= \frac{a_{2i-1, 2j-1} + a_{2i-1, 2j} + a_{2i, 2j-1} + a_{2i, 2j}}{2}, \\
 \mathcal{B}_2(i, j) &= \frac{a_{2i-1, 2j} + a_{2i, 2j} - a_{2i-1, 2j-1} - a_{2i, 2j-1}}{2}, \\
 \mathcal{B}_3(i, j) &= \frac{a_{2i, 2j-1} + a_{2i, 2j} - a_{2i-1, 2j-1} - a_{2i-1, 2j}}{2}, \\
 \mathcal{B}_4(i, j) &= \frac{a_{2i-1, 2j-1} + a_{2i, 2j} - a_{2i-1, 2j} + a_{2i, 2j-1}}{2},
 \end{aligned} \tag{11}$$

implicating that each wavelet coefficient is the sum of four $M/2 \times N/2$ matrices. Consequently, the computational complexity of the 2-D HWT via this method is diminished to $O(\frac{3}{4}MN)$, with the 2-D IHWT exhibiting the same complexity of $O(\frac{3}{4}MN)$ upon analogous considerations.

4 Haar Nuclear Norm

4.1 Motivation

The 2-D HWT decomposes an image into an approximation coefficient and three detail coefficients, and it has achieved significant advancements in image processing. However, it's unclear if these coefficients maintain low-rank properties for low-rank data, which this section explores.

The image considered in this paper is structured as a 3-order tensor, $\mathcal{A} \in \mathbb{R}^{M \times N \times S}$, with $M \times N$ pixels and S channels. Our focus is on characterizing spatial contents, which can be achieved through wavelet decomposition along the first and second modes. Consequently, the 2-D HWT for tensor images is defined as follows:

Definition 5 (2-D Frontal Slice-wise Haar Discrete Wavelet Transform). *Given a 3-order tensor $\mathcal{A} \in \mathbb{R}^{M \times N \times S}$, the 2-D frontal slice-wise HWT (FHWT) is defined as:*

$$\mathcal{B} = \mathcal{F}(\mathcal{A}) = \mathcal{A} \times_1 \mathbf{W}_M \times_2 \mathbf{W}_N. \tag{12}$$

Equivalently, $\mathcal{B}(:, :, k) = F(\mathcal{A}(:, :, k)) = \mathbf{W}_M \mathcal{A}(:, :, k) \mathbf{W}_N^T$. That is, 2-D FHWT is equivalent to applying 2-D HWT to each frontal slice of the tensor. The 2-D inverse FHWT (IFHWT) is given by:

$$\mathcal{A} = \mathcal{F}^{-1}(\mathcal{B}) = \mathcal{B} \times_1 \mathbf{W}_M^T \times_2 \mathbf{W}_N^T. \tag{13}$$

The wavelet coefficient \mathcal{B} can be represented as a block tensor comprising four wavelet coefficient tensors $\mathcal{B}_i \in \mathbb{R}^{M/2 \times N/2 \times S}$ ($i = 1, 2, 3, 4$):

$$\begin{aligned}
 \mathcal{B} &= \mathcal{A} \times_1 \mathbf{W}_M \times_2 \mathbf{W}_N \\
 &= \mathcal{A} \times_1 \begin{bmatrix} \mathbf{H}_{M/2} \\ \mathbf{G}_{M/2} \end{bmatrix} \times_2 \begin{bmatrix} \mathbf{H}_{N/2} \\ \mathbf{G}_{N/2} \end{bmatrix} \\
 &\triangleq \begin{bmatrix} \mathcal{F}_1(\mathcal{A}) & \mathcal{F}_2(\mathcal{A}) \\ \mathcal{F}_3(\mathcal{A}) & \mathcal{F}_4(\mathcal{A}) \end{bmatrix} \triangleq \begin{bmatrix} \mathcal{B}_1 & \mathcal{B}_2 \\ \mathcal{B}_3 & \mathcal{B}_4 \end{bmatrix}.
 \end{aligned} \tag{14}$$

In this equation, $\mathcal{F}_i(\mathcal{A})$ represents a mapping from tensor \mathcal{A} to the i -th wavelet coefficient tensor. It is noteworthy that the wavelet coefficients can be considered as the sum of four $M/2 \times N/2 \times S$ tensors (as detailed in the analysis near Eq. 11), thus the computational complexity of 2-D FHWT (or IFHWT) is $O(\frac{3}{4}MNS)$.

If the original image is LR, its wavelet coefficients are intuitively also LR. This is supported by Fig. 1(a), showing fast-decaying singular values across all wavelet coefficients. Furthermore, the following theorem delineates the low-rank property of the wavelet coefficients \mathcal{B}_i :

Theorem 6 (Low-rank Properties for Wavelet Coefficients). *Consider a 3-order tensor $\mathcal{A} \in \mathbb{R}^{M \times N \times S}$. Let $[\mathcal{B}_1, \mathcal{B}_2; \mathcal{B}_3, \mathcal{B}_4] = \text{FHWT}_2(\mathcal{A})$, and then there is*

$$\text{rank}_n(\mathcal{B}_i) \leq \text{rank}_n(\mathcal{A}), \tag{15}$$

for $n = 1, 2, 3$ and $i = 1, 2, 3, 4$.

The proof is provided in the supplementary materials. The theorem states that the Tucker rank of the wavelet coefficients does not exceed

that of the original data, confirming that wavelet coefficients remain LR if the original data is LR.

Cumulative energy (CE) curves provide more insights into the singular value distributions of wavelet coefficients. For a singular value sequence of length n , $(\lambda_1, \dots, \lambda_n)$, the k -th CE is calculated as the ratio of the cumulative sum of the first k singular values to the total sum of singular values, $CE_k = \frac{\sum_{i=1}^k \lambda_i}{\sum_{i=1}^n \lambda_i}$. Fig. 1(b) shows that the CE curve for the approximation coefficient \mathcal{B}_1 rises faster than those for the detail coefficients $\mathcal{B}_i (i = 2, 3, 4)$. This suggests that the singular values of low-frequencies are less dispersed, allowing for reconstruction with fewer principal components. In contrast, the singular values of high-frequencies are more dispersed, needing more components for reconstruction. Consequently, coarse-grained structures are more low-rank, while fine-grained details are less so. The original image, a mix of low- and high-frequencies, has a CE curve that falls between those of the low- and high-frequencies, indicating it is of intermediate low-rank.

NN/TNN applies LR regularization to the original image without considering the distinct singular value distributions of low- and high-frequencies, potentially leading to insufficient detail preservation. CTV/TCTV focuses on high-frequencies through gradient operators, ensuring their preservation but possibly inaccurately modeling the LR prior for coarse structures and risking color or spectral distortions.

4.2 Haar nuclear norm

This paper introduces the Haar Nuclear Norm (HNN) to model the disentangled LR properties of low- and high-frequency wavelet coefficients.

Definition 7. Given a 3-order tensor $\mathcal{A} \in \mathbb{R}^{M \times N \times S}$, let $[\mathcal{B}_1, \mathcal{B}_2; \mathcal{B}_3, \mathcal{B}_4] = \text{FHWT}_2(\mathcal{A})$, and HNN is defined as the sum of the nuclear norms of the mode-3 unfoldings of all wavelet coefficients,

$$\|\mathcal{A}\|_{\text{HNN}} = \sum_{i=1}^4 \|(\mathcal{B}_i)_{(3)}\|_*. \quad (16)$$

It is crucial to clarify the distinction between HNN and existing methods. Firstly, as illustrated in Fig. 1, the existing tools primarily concentrate on LR recovery either in the original image domain (e.g., TNN) or the transformed domain (e.g., TCTV). The former is good at recovering coarse-grained structure but the entangled LR modeling may neglect detail preservation, while the latter maintains fine-grained details but may lack robust structure recovery. HNN differs from existing methods by explicitly modeling the LR properties of disentangled coarse-grained structures (approximation coefficients) and fine-grained textures (detail

coefficients). It offers a balance between structure recovery and detail preservation, potentially outperforming methods like TNN and TCTV.

Despite involving the NN of four wavelet coefficients, HNN does not significantly increase computational burden. The most intensive operations are SVD and 2-D FHWT/IFHWT, with complexities of $O(MNS^2)$ and $O(\frac{3}{4}MNS)$, respectively. Since $\frac{3}{4}MNS \ll MNS^2$, the 2-D FHWT/IFHWT is negligible compared to SVD, making HNN only slightly slower than the NN in terms of computational complexity. However, TNN and TCTV involve additional complexities due to the fast Fourier transform, $O(MNS \log S)$ and $O(MNS \log MNS)$, respectively. Consequently, HNN is expected to be more computationally efficient than TNN and TCTV.

4.3 HNN based matrix completion

The HNN based matrix completion (HNN-MC) problem is formulated as

$$\min_{\mathcal{X}} \|\mathcal{X}\|_{\text{HNN}}, \text{ s.t. } \mathcal{P}_{\Omega}(\mathcal{M}) = \mathcal{P}_{\Omega}(\mathcal{X}). \quad (17)$$

Note that remote sensing imagery is often written in a tensor format. By introducing auxiliary variables \mathcal{E} , it can be rewritten as

$$\begin{cases} \min_{\mathcal{X}} \sum_{i=1}^4 \|(\mathcal{B}_i)_{(3)}\|_*, \\ \text{s.t. } \mathcal{M} = \mathcal{X} + \mathcal{E}, \mathcal{P}_{\Omega}(\mathcal{E}) = 0, \mathcal{B}_i = \mathcal{F}_i(\mathcal{X}). \end{cases} \quad (18)$$

Recall that $\mathcal{F}_i(\mathcal{X})$ denotes a mapping from a tensor \mathcal{A} into the i -th wavelet coefficient, defined in Eq. (14).

The ADMM algorithm is then exploited to solve the issue, and the corresponding augmented Lagrangian function is

$$\begin{aligned} \mathcal{L} = & \left(\sum_{i=1}^4 \|(\mathcal{B}_i)_{(3)}\|_* + \frac{\mu_b}{2} \left\| \mathcal{B}_i - \mathcal{F}_i(\mathcal{X}) + \frac{\Gamma_i}{\mu_b} \right\|_F^2 \right) \\ & + \frac{\mu_a}{2} \left\| \mathcal{M} - \mathcal{X} - \mathcal{E} + \frac{\Gamma_5}{\mu_a} \right\|_F^2, \end{aligned} \quad (19)$$

with a constraint $\mathcal{P}_{\Omega}(\mathcal{E}) = 0$, where μ_a and μ_b are penalty parameters, and $\Gamma_i \in \mathbb{R}^{M/2 \times N/2 \times S} (i = 1, 2, 3, 4)$ and $\Gamma_5 \in \mathbb{R}^{M \times N \times S}$ are Lagrangian multipliers. In the ADMM, each unknown variable is updated iteratively by fixing others, and the updating equations are discussed as follows:

Update \mathcal{E} : Fixing other variables, the optimization problem of \mathcal{E} is given by

$$\min_{\mathcal{E}} \left\| \mathcal{E} - \left(\mathcal{M} - \mathcal{X} + \frac{\Gamma_5}{\mu_a} \right) \right\|_2^2, \text{ s.t. } \mathcal{P}_{\Omega}(\mathcal{E}) = 0, \quad (20)$$

This is a constrained least squares problem, and the solution is given by

$$\mathcal{E} = \mathcal{P}_{\Omega^\perp} \left(\mathcal{M} - \mathcal{X} + \frac{\Gamma_5}{\mu_a} \right), \quad (21)$$

where Ω^\perp is the complement set of Ω .

Update \mathcal{B}_i : Fixing other variables, the optimization problem of \mathcal{B}_i is written as

$$\min_{\mathcal{B}_i} \left\| (\mathcal{B}_i)_{(3)} \right\|_* + \frac{\mu_b}{2} \left\| \mathcal{B}_i - \mathcal{F}_i(\mathcal{A}) + \frac{\Gamma_i}{\mu_b} \right\|_F^2. \quad (22)$$

The solution is given by singular value thresholding,

$$\mathcal{B}_i = \text{fold}_3 \left(\mathbf{U} \mathcal{G}_{1/\mu_b}(\boldsymbol{\Sigma}) \mathbf{V}^T \right), \quad (23)$$

where $[\mathbf{U}, \boldsymbol{\Sigma}, \mathbf{V}^T] \triangleq \text{svd}(\mathcal{F}_i(\mathcal{A}) - \Gamma_i/\mu_b)$, and $\mathcal{G}_\gamma(a) = \text{sign}(a) \max(|a| - \gamma, 0)$ denotes the soft-thresholding function.

Update \mathcal{X} : Fixing other variables, the optimization problem of \mathcal{X} is given by

$$\min_{\mathcal{X}} \frac{\mu_b}{2} \left\| \mathcal{B} - \mathcal{F}(\mathcal{X}) + \frac{\Gamma}{\mu_b} \right\|_F^2 + \frac{\mu_a}{2} \left\| \mathcal{M} - \mathcal{X} - \mathcal{E} + \frac{\Gamma_5}{\mu_a} \right\|_F^2. \quad (24)$$

This is a weighted least squares problem, and it is easy to compute the gradient of this loss function regarding \mathcal{X} ,

$$\begin{aligned} & \frac{\partial \mathcal{L}(\mathcal{X})}{\partial \mathcal{X}} \\ &= \mu_a (\mathcal{X} + \mathcal{E} - \mathcal{M} - \Gamma_5/\mu_a) + \mu_b (\mathcal{X} \times_1 \mathbf{W}_M \times_2 \mathbf{W}_N \\ & \quad - \mathcal{B} - \frac{\Gamma}{\mu_b}) \times_1 \mathbf{W}_M^T \times_2 \mathbf{W}_N^T \\ &= \mu_a (\mathcal{X} + \mathcal{E} - \mathcal{M} - \Gamma_5/\mu_a) + \mu_b \mathcal{X} - \mathcal{F}^{-1}(\mu_b \mathcal{B} + \Gamma). \end{aligned}$$

Let the gradient be zero, and the solution is

$$\mathcal{X} = \frac{\mu_a (\mathcal{M} + \Gamma_5/\mu_a - \mathcal{E}) + \mathcal{F}^{-1}(\mu_b \mathcal{B} + \Gamma)}{\mu_a + \mu_b}. \quad (25)$$

Except for the aforementioned variables, the multipliers and penalty parameters are updated by

$$\begin{aligned} \Gamma_i &= \Gamma_i + \mu_b (\mathcal{B}_i - \mathcal{F}_i(\mathcal{X})), \quad (i = 1, 2, \dots, 4) \\ \Gamma_5 &= \Gamma_5 + \mu_a (\mathcal{M} - \mathcal{X} - \mathcal{E}), \quad \mu_a = \mu_a \rho, \quad \mu_b = \mu_b \rho, \end{aligned} \quad (26)$$

where ρ is constant greater than 1.

4.4 HNN based robust principal component analysis

Given a noisy observation \mathcal{M} , it is assumed that \mathcal{M} can be decomposed a low-rank component \mathcal{X} (i.e., clean data) and a sparse noise component \mathcal{S} . The HNN based robust principal component analysis (HNN-RPCA) problem tries to recover \mathcal{X} ,

formulated as

$$\min_{\mathcal{X}} \|\mathcal{X}\|_{\text{HNN}} + \lambda \|\mathcal{E}\|_1, \quad \text{s.t. } \mathcal{M} = \mathcal{X} + \mathcal{E}. \quad (27)$$

With the definition of HNN, it is rewritten as

$$\begin{cases} \min_{\mathcal{X}} \sum_{i=1}^4 \|(\mathcal{B}_i)_{(3)}\|_* + \lambda \|\mathcal{E}\|_1, \\ \text{s.t. } \mathcal{M} = \mathcal{X} + \mathcal{E}, \mathcal{B}_i = \mathcal{F}_i(\mathcal{X}). \end{cases} \quad (28)$$

Its augmented Lagrangian function is

$$\begin{aligned} \mathcal{L} &= \left(\sum_{i=1}^4 \|(\mathcal{B}_i)_{(3)}\|_* + \frac{\mu_b}{2} \left\| \mathcal{B}_i - \mathcal{F}_i(\mathcal{X}) + \frac{\Gamma_i}{\mu_b} \right\|_F^2 \right) \\ & \quad + \lambda \|\mathcal{E}\|_1 + \frac{\mu_a}{2} \left\| \mathcal{M} - \mathcal{X} - \mathcal{E} + \frac{\Gamma_5}{\mu_a} \right\|_F^2, \end{aligned} \quad (29)$$

where μ_a and μ_b are penalty parameters, and $\Gamma_i \in \mathbb{R}^{M/2 \times N/2 \times S}$ ($i = 1, 2, 3, 4$) and $\Gamma_5 \in \mathbb{R}^{M \times N \times S}$ are Lagrangian multipliers. The solution is very similar to that of HNN based image inpainting, as follows:

$$\begin{cases} \mathcal{E} = \mathcal{G}_{\lambda/\mu_a} \left(\mathcal{M} - \mathcal{X} + \frac{\Gamma_5}{\mu_a} \right), \\ \mathcal{B}_i = \text{fold}_3 \left(\mathbf{U} \mathcal{G}_{1/\mu_b}(\boldsymbol{\Sigma}) \mathbf{V}^T \right), \\ \mathcal{X} = \frac{\mu_a (\mathcal{M} + \Gamma_5/\mu_a - \mathcal{E}) + \mathcal{F}^{-1}(\mu_b \mathcal{B} + \Gamma)}{\mu_a + \mu_b}, \\ \Gamma_i = \Gamma_i + \mu_b (\mathcal{B}_i - \mathcal{F}_i(\mathcal{X})), \quad (i = 1, 2, \dots, 4) \\ \Gamma_5 = \Gamma_5 + \mu_a (\mathcal{M} - \mathcal{X} - \mathcal{E}), \\ \mu_a = \mu_a \rho, \quad \mu_b = \mu_b \rho. \end{cases} \quad (30)$$

5 Theory of Recovery Guarantee

The section develops the theory of recovery guarantee for HNN-RPCA and HNN-TC models. To ease representation, this section would use the matrix notations. Firstly, incoherence conditions on the transformed maps after Haar transformation are defined. Specifically, assuming that each transformed map $(\mathcal{B}_i)_{(3)} \in \mathbb{R}^{M \times N/4 \times S}$, ($i = 1, \dots, 4$) of $\mathbf{X}_0 \in \mathbb{R}^{M \times N \times S}$ with rank of r has the singular value decomposition $\mathbf{U}_i \boldsymbol{\Sigma}_i \mathbf{V}_i^T$, where $\mathbf{U}_i \in \mathbb{R}^{M \times r}$ and $\mathbf{V}_i \in \mathbb{R}^{S \times r}$, the incoherence condition with a fixed constant μ is defined as follows:

$$\max_k \|\mathbf{U}_i^T \hat{e}_k\|^2 \leq \frac{\mu r}{n_1}, \quad i = 1, \dots, 4. \quad (31)$$

$$\max_k \|\mathbf{V}_i^T \hat{e}_k\|^2 \leq \frac{\mu r}{n_2}, \quad i = 1, \dots, 4. \quad (32)$$

$$\|\mathbf{U}_i \mathbf{V}_i^T\|_\infty \leq \sqrt{\frac{\mu r}{n_1 n_2}}, \quad i = 1, \dots, 4. \quad (33)$$

Here, $\|\mathbf{X}\|_\infty = \max_{i,j} |\mathbf{X}_{i,j}|$, and \hat{e}_k is the standard orthonormal basis. The exact decomposition

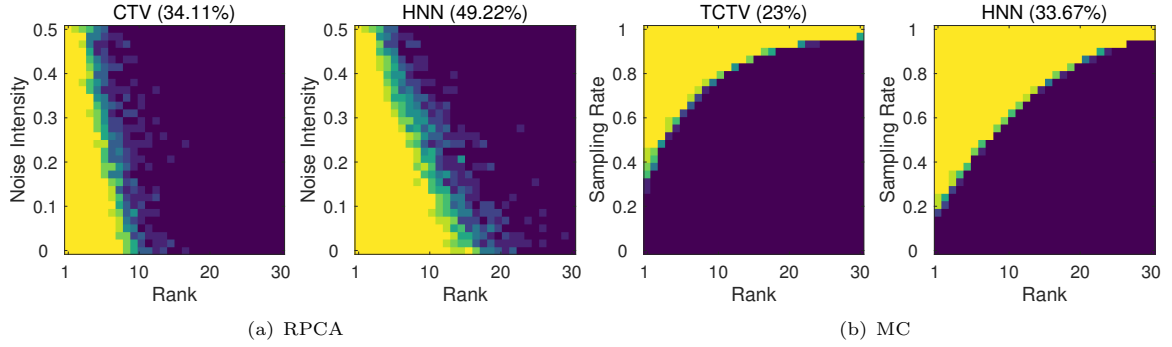


Fig. 2 Phase transitions of (a) RPCA models and (b) MC models. The success rates are shown in the title of each panel.

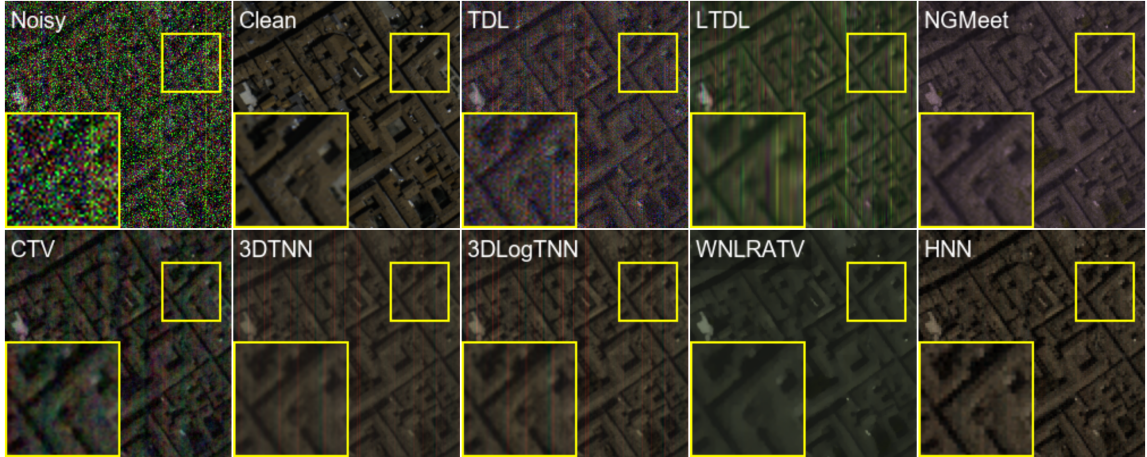


Fig. 3 The false-color denoised images (band 24-17-1) of compared methods on the PC dataset for case 6.

theorem for HNN-RPCA model is derived as follows, where we now write it in matrix notations,

$$\min_{\mathbf{X}} \|\mathbf{X}\|_{\text{HNN}} + \lambda \|\mathbf{E}\|_1, \text{ s.t. } \mathbf{M} = \mathbf{X} + \mathbf{E}. \quad (34)$$

Theorem 8 (HNN-RPCA Theorem). *Suppose that the transformed map $(\mathbf{B}_i)_{(3)} \in \mathbb{R}^{MN/4 \times S}$, $(i = 1, \dots, 4)$ of $\mathbf{X}_0 \in \mathbb{R}^{MN \times S}$ with rank r satisfies the incoherence conditions (31)-(33), and the support set Ω of \mathbf{E}_0 is uniformly distributed over all sets of cardinality m . Then, with a probability of at least $1 - cn_{(1)}^{-10}$ (for the choice of support set exceeding \mathbf{E}_0), the HNN-RPCA model with $\lambda = 4/\sqrt{n_{(1)}}$ guarantees an exact recovery, i.e., the minimization in Eq. (34) yields $\hat{\mathbf{X}} = \mathbf{X}_0$ and $\hat{\mathbf{E}} = \mathbf{E}_0$, provided that:*

$$\text{rank}(\mathbf{X}_0) \leq \rho_r n_2 \mu^{-1} (\log n_{(1)})^{-2}, m \leq \rho_s n_1 n_2. \quad (35)$$

Here, ρ_r and ρ_s are numerical constants, where ρ_s determines the sparsity of \mathbf{E}_0 , ρ_r is a small constant related to the rank of \mathbf{X}_0 , and $n_{(1)} = \max\{MN/4, S\}$.

Similarly, for the HNN-MC model which is written in matrix notations as:

$$\min_{\mathbf{X}} \|\mathbf{X}\|_{\text{HNN}}, \text{ s.t. } \mathcal{P}_{\Omega}(\mathbf{M}) = \mathcal{P}_{\Omega}(\mathbf{X}), \quad (36)$$

there is the following theorem.

Theorem 9 (HNN-MC Theorem). *Suppose that $\mathbf{B}_i \in \mathbb{R}^{MN/4 \times S}$, $(i = 1, \dots, 4)$ obey the incoherence conditions (31)-(32), $\Omega \sim \text{Ber}(p)$ and m is the number of Ω , where $\text{Ber}(p)$ represents the Bernoulli distribution with parameter p . Let $n_1 = MN/4$ and $n_2 = S$, and without loss of generality, suppose $n_1 \geq n_2$. Then, there exist universal constants $c_0, c_1 > 0$ such that \mathbf{X}_0 is the unique solution to MNN-MC model (36) with probability at least $1 - c_1 n_1^{-3} \log n_1$, provided that*

$$m \geq c_0 \mu r n_1^{5/4} \log(n_1). \quad (37)$$

The proofs of the above theorems are placed in the supplementary material. These theorems show that the HNN-RPCA/-MC model has the exact recovery with a high probability.

6 Experiments

The proposed model's effectiveness is tested through extensive experiments using four quality metrics: Peak Signal-to-Noise Ratio (PSNR), Structural Similarity (SSIM), Erreur Relative Globale Adimensionnelle de Synthèse (ERGAS), and Spectral Angle Mapper (SAM). PSNR, SSIM, and ERGAS evaluate spatial distortion, while SAM measures spectral distortion. Better image quality is indicated by higher PSNR and SSIM scores, and lower ERGAS and SAM scores. Experiments were

Table 1 HSI denoising metrics on the BA dataset. The best and the second best results are highlighted in **bold** and underline, respectively.

Case	Metrics	Noisy	LLRT	TDL	LTDL	NGMeet	CTV	3DTNN	3DLogTNN	WNLRAV	RCILD	HNN
1	PSNR \uparrow	13.06	15.6	22.9	23.04	23.15	27.95	26.7	24.42	<u>28.37</u>	23.22	31.89
	SSIM \uparrow	0.0308	0.062	0.6801	0.7085	0.7408	0.4991	0.5886	0.3614	<u>0.7549</u>	0.7381	0.7864
	ERGAS \downarrow	1114.99	838.17	416.67	414.47	411.94	<u>196.53</u>	256.8	303.19	210.78	411.8	126.5
	SAM \downarrow	0.269	0.217	0.083	0.082	0.081	0.091	<u>0.080</u>	0.108	0.087	0.082	0.045
2	PSNR \uparrow	14.3	16.63	24.18	25.66	24.38	<u>29.17</u>	28.15	26.36	28.84	26.13	32.16
	SSIM \uparrow	0.0467	0.0847	0.5333	0.748	0.7006	0.5677	0.6416	0.4666	0.7405	<u>0.7892</u>	0.8064
	ERGAS \downarrow	1046.25	818.79	412.75	365.74	406.52	<u>174.26</u>	230.81	277.38	219.36	361.53	129.73
	SAM \downarrow	0.266	0.221	0.099	0.086	0.100	0.080	<u>0.076</u>	0.106	0.092	0.085	0.047
3	PSNR \uparrow	13.33	15.77	22.82	23.77	23.12	<u>29.23</u>	25.05	21.35	28.48	24.91	32.02
	SSIM \uparrow	0.0408	0.0772	0.4622	0.7111	0.6552	0.5706	0.329	0.1923	0.7041	<u>0.7612</u>	0.802
	ERGAS \downarrow	1195.65	932.48	471.94	436.95	463.06	<u>170.52</u>	295.23	476.74	248.07	409.96	130.87
	SAM \downarrow	0.278	0.232	0.108	0.096	0.107	<u>0.081</u>	0.119	0.178	0.106	0.094	0.049
4	PSNR \uparrow	14.35	16.68	23.96	25.36	24.6	29.1	27.45	24.89	<u>29.58</u>	26.52	32.26
	SSIM \uparrow	0.0473	0.0862	0.5004	0.742	0.7169	0.564	0.5438	0.3648	0.7839	<u>0.7972</u>	0.8079
	ERGAS \downarrow	1024.37	797.55	401.08	362.24	386.97	<u>174.07</u>	234.16	313.58	198.36	336.48	125.28
	SAM \downarrow	0.265	0.220	0.099	0.084	0.096	<u>0.080</u>	0.084	0.122	0.084	0.082	0.046
5	PSNR \uparrow	14.86	17.22	21.92	23.48	25.74	<u>27.35</u>	26.74	<u>27.42</u>	26.34	26.72	29.16
	SSIM \uparrow	0.0525	0.0971	0.2834	0.6506	<u>0.7111</u>	0.5363	0.6656	0.6634	0.567	0.7472	0.6868
	ERGAS \downarrow	978.93	766.22	472.17	273.05	353.64	<u>235.23</u>	267.21	256.9	314.17	309.07	219.12
	SAM \downarrow	0.276	0.233	0.154	0.084	0.111	0.123	0.108	0.110	0.148	<u>0.095</u>	0.105
6	PSNR \uparrow	13.47	15.97	20.75	21.46	24.1	<u>27.25</u>	26.45	25.35	25.78	25.11	28.99
	SSIM \uparrow	0.0417	0.0817	0.2425	0.5546	0.6633	0.5288	0.5819	0.4671	0.5201	0.7145	<u>0.67</u>
	ERGAS \downarrow	1154.8	892.02	524.67	332.13	422.28	<u>234.78</u>	260.3	298.07	368.66	380.11	224.18
	SAM \downarrow	0.288	0.242	0.153	0.096	0.115	0.122	0.110	0.131	0.171	0.111	<u>0.108</u>

Table 2 HSI denoising metrics on the PC dataset. The best and the second best results are highlighted in **bold** and underline, respectively.

Case	Metrics	Noisy	LLRT	TDL	LTDL	NGMeet	CTV	3DTNN	3DLogTNN	WNLRAV	RCILD	HNN
1	PSNR \uparrow	12.54	16.96	23.35	23.04	23.92	25.95	25.12	<u>27.04</u>	24.02	24.04	27.59
	SSIM \uparrow	0.117	0.255	0.7348	0.7085	0.7947	0.7116	0.7288	<u>0.8074</u>	0.7155	0.8061	0.8099
	ERGAS \downarrow	865.04	521.08	255.24	414.47	241.74	185.14	204.08	<u>165.22</u>	233.17	238.13	152.69
	SAM \downarrow	0.243	0.155	0.047	0.082	0.043	0.081	<u>0.042</u>	0.039	0.047	0.043	0.044
2	PSNR \uparrow	14.17	17.98	22.66	25.66	24.37	27.6	27.13	<u>28.16</u>	27.45	25.94	28.45
	SSIM \uparrow	0.1789	0.3117	0.5653	0.748	0.7478	0.783	0.7706	0.7953	0.8035	0.8471	<u>0.8452</u>
	ERGAS \downarrow	773.26	505.14	302.96	365.74	257.31	<u>155.13</u>	166.15	157.8	178.52	207.37	139.07
	SAM \downarrow	0.234	0.163	0.091	0.086	0.073	0.070	0.054	0.062	0.056	<u>0.049</u>	0.044
3	PSNR \uparrow	13.5	17.39	22.05	23.77	23.44	27.86	27.31	28.36	27.06	24.86	<u>28.24</u>
	SSIM \uparrow	0.1609	0.2901	0.535	0.7111	0.7168	0.794	0.7805	0.8013	0.7725	<u>0.8227</u>	0.8404
	ERGAS \downarrow	842.82	554.27	326.73	436.95	316.19	<u>150.55</u>	162.93	161.15	254.39	252.96	145.68
	SAM \downarrow	0.242	0.173	0.093	0.096	0.086	0.069	<u>0.054</u>	0.065	0.079	0.061	0.048
4	PSNR \uparrow	13.12	17.28	22.08	25.36	23.7	26.45	25.17	<u>27.03</u>	25.25	25.73	27.76
	SSIM \uparrow	0.1369	0.2721	0.5492	0.742	0.7483	0.7374	0.7312	0.8083	0.7293	0.8391	<u>0.8186</u>
	ERGAS \downarrow	835.9	521.79	304.17	362.24	259.7	175.11	203.36	<u>165.42</u>	214.67	214.09	149.84
	SAM \downarrow	0.241	0.161	0.081	0.084	0.064	0.078	<u>0.044</u>	0.042	0.056	0.052	0.045
5	PSNR \uparrow	13.52	17.6	19.86	23.55	24.02	24.13	23.91	25.11	25.16	25.6	<u>25.43</u>
	SSIM \uparrow	0.1468	0.28	0.3895	0.5351	0.7315	0.662	0.6469	0.6957	0.7094	0.7664	<u>0.7447</u>
	ERGAS \downarrow	813.08	510.51	399.92	406.29	255.25	263.17	266.18	252.27	242.79	227.82	<u>241.2</u>
	SAM \downarrow	0.252	0.173	0.136	0.124	<u>0.080</u>	0.115	0.092	0.096	0.087	0.080	0.094
6	PSNR \uparrow	12.96	17.12	19.21	22.3	23.56	24.02	23.29	<u>24.23</u>	23.64	23.79	24.88
	SSIM \uparrow	0.1353	0.2645	0.3528	0.472	<u>0.7248</u>	0.6633	0.6065	0.6518	0.5969	0.7171	0.7288
	ERGAS \downarrow	875.19	552.58	433.47	460.26	287.06	270.3	280.32	271.1	287.3	259.8	<u>260.4</u>
	SAM \downarrow	0.260	0.183	0.145	0.133	<u>0.092</u>	0.119	0.098	0.105	0.092	0.085	0.108

conducted on a Windows 11 desktop with an 8-core R7-4800H CPU and 16GB RAM.

6.1 Experiments on phase transition

The recovery phenomenon was analyzed across varying Tucker ranks and noise intensities of \mathbf{E} for RPCA problems, or varying sampling rates of \mathbf{M} for MC problems. A simulated tensor $\mathcal{X} \in \mathbb{R}^{30 \times 30 \times 30}$ was generated using the equation $\mathcal{X} = \mathcal{C} \times_1 \mathbf{U}_1 \times_2 \mathbf{U}_2 \times_3 \mathbf{U}_3$, where $\mathcal{C} \in \mathbb{R}^{R \times R \times R}$ and $\mathbf{U}_i \in \mathbb{R}^{30 \times R}$, for $i = 1, 2, 3$. The rank R varied from 1 to 30, the noise intensity ranged from 0.01 to 0.5,

and the sampling rate varied from 0.01 to 0.99. For each case, the experiment was repeated 10 times, and a trial was deemed successful if the average relative reconstruction error was less than 0.1. Figure 2 illustrates the phase transition maps (yellow = 100%, blue = 0%), indicating that HNN achieved a higher success rate than CTV and TCTV.

6.2 Experiments on HSI denoising

This section carries out HSI denoising experiments to assess the performance of HNN based RPCA. The compared methods include non-local meets

Table 3 Metrics for HSI inpainting on the BA dataset. The best and the second best results are highlighted in **bold** and underline, respectively.

SR	Metrics	Observed	SNN	KBR	TNN	SPCTV	TNNTV	FCTNTC	FCTNFR	TCTV	HNN
7%	PSNR \uparrow	20.09	31.82	<u>44.88</u>	39.47	40.07	34.05	37.06	39.89	44.43	48.46
	SSIM \uparrow	0.0864	0.8254	0.9742	0.9314	0.9492	0.8542	0.8920	0.9385	<u>0.9749</u>	0.9898
	ERGAS \downarrow	535.81	138.69	<u>31.90</u>	61.77	52.10	108.97	73.48	52.66	33.26	22.30
	SAM \downarrow	1.3075	0.1374	<u>0.0397</u>	0.0857	0.0632	0.0962	0.0859	0.0643	0.0456	0.0288
5%	PSNR \uparrow	20.00	31.10	41.46	36.83	37.67	33.15	36.89	39.40	<u>42.40</u>	45.55
	SSIM \uparrow	0.0708	0.8145	0.9501	0.8908	0.9215	0.8412	0.8883	0.9316	<u>0.9616</u>	0.9824
	ERGAS \downarrow	541.57	150.60	47.38	85.19	69.13	121.79	74.92	55.64	<u>43.01</u>	30.77
	SAM \downarrow	1.3515	0.1489	0.0534	0.1173	0.0802	0.1059	0.0871	0.0669	<u>0.0576</u>	0.0396
4%	PSNR \uparrow	19.95	30.74	39.20	35.17	36.14	32.70	36.72	39.05	<u>39.76</u>	43.00
	SSIM \uparrow	0.0623	0.8097	0.9267	0.8587	0.8993	0.8343	0.8852	0.9258	<u>0.9375</u>	0.9688
	ERGAS \downarrow	544.37	156.67	61.55	103.90	82.73	128.49	76.36	57.91	<u>55.64</u>	43.63
	SAM \downarrow	1.3764	0.1546	<u>0.0665</u>	0.1425	0.0927	0.1125	0.0890	0.0691	0.0722	0.0576

Table 4 Metrics for HSI inpainting on the PC dataset. The best and the second best results are highlighted in **bold** and underline, respectively.

SR	Metrics	Observed	SNN	KBR	TNN	SPCTV	TNNTV	FCTNTC	FCTNFR	TCTV	HNN
7%	PSNR \uparrow	14.68	21.72	<u>36.95</u>	31.17	30.34	22.44	28.94	33.56	32.79	38.37
	SSIM \uparrow	0.0380	0.3756	<u>0.9678</u>	0.8822	0.8749	0.3975	0.8165	0.9288	0.9228	0.9799
	ERGAS \downarrow	722.79	319.96	<u>56.13</u>	118.83	119.25	294.82	139.44	83.19	92.52	49.24
	SAM \downarrow	1.3109	0.1961	<u>0.0806</u>	0.1845	0.1369	0.1757	0.1742	0.1213	0.1513	0.0559
5%	PSNR \uparrow	14.59	21.25	31.38	28.69	27.72	21.89	28.60	<u>32.53</u>	30.86	35.04
	SSIM \uparrow	0.0287	0.3399	0.8912	0.8157	0.7863	0.3529	0.8041	<u>0.9114</u>	0.8861	0.9594
	ERGAS \downarrow	730.54	337.91	105.51	152.20	160.69	313.87	144.82	<u>92.98</u>	113.63	72.15
	SAM \downarrow	1.3557	0.1931	<u>0.1141</u>	0.2003	0.1556	0.1703	0.1777	0.1272	0.1763	0.0717
4%	PSNR \uparrow	14.54	21.04	28.58	26.91	25.97	21.67	28.31	<u>31.68</u>	29.75	32.10
	SSIM \uparrow	0.0240	0.3255	0.8091	0.7446	0.7007	0.3344	0.7929	<u>0.8947</u>	0.8578	0.9225
	ERGAS \downarrow	734.34	346.05	145.46	183.00	196.45	322.02	149.69	<u>102.09</u>	128.31	103.87
	SAM \downarrow	1.3823	0.1896	<u>0.1295</u>	0.2039	0.1656	0.1681	0.1831	0.1358	0.1911	0.0952

global (NGMeet) [9], hyper-Laplacian regularized unidirectional low-rank tensor recovery (LLRT) [1], tensor dictionary learning (TDL) [26], CTV [24], three-directional TNN (3DTNN) [46], 3D log-based TNN (3DLogTNN) [46], and weighted non-local low-rank model with adaptive TV regularization (WNLRTV) [2]. Besides them, it is also compared with a deep learning based method, representative coefficient image with a learnable denoiser (RCILD) [23]. The experiments simulate six scenarios:

1. Case 1: I.i.d. Gaussian noise with $\sigma = 75$;
2. Case 2: Non-i.i.d. Gaussian noise with band-varying standard deviations $\sigma \in [30, 100]$;
3. Case 3: Building on Case 2, 1/3 of the bands are corrupted by impulse noise with varying ratios $p \in [5\%, 20\%]$;
4. Case 4: Building on Case 2, 1/3 of the bands are corrupted by stripe noise with varying ratios $p \in [5\%, 20\%]$;
5. Case 5: Building on Case 2, 1/3 of the bands are corrupted by deadline noise with varying ratios $p \in [5\%, 20\%]$;
6. Case 6: Building on Case 2, the data is corrupted by a mixture of impulse, stripe, and deadline noise as described in the preceding cases.

Tables 1 and 2 list the HSI denoising metrics on the BA and PC datasets, respectively. The noise intensity in this experiment configuration is severe, but HNN still exhibits robust performance. Notably, it surpasses CTV in terms of PSNR, with an improvement of 1.74 dB on the BA datasets for case 6. Visual inspection of the results in Fig. 3 reveals that methods including TDL, LTDL, CTV, 3DTNN and 3DLogTNN exhibit noticeable noise. Although NGMeet and WNLRTV effectively remove noise, they suffer from spectral distortion, due to the color mismatch. HNN stands out by generating an image that closely aligns with the ground truth.

6.3 Experiments on HSI inpainting

This subsection focuses on HSI inpainting, and we conduct experiments using the Bay Area (BA) and Pavia Center (PC) datasets. The BA dataset has dimensions of $256 \times 256 \times 193$, while the PC dataset has dimensions of $200 \times 200 \times 80$. We compare the HNN method with eight methods, including SNN [17], TNN [19], TCTV [31], Kronecker-Basis-Representation (KBR) [33], TNNTV [27], FCTN based tensor completion (FCTNTC) [48], FCTN

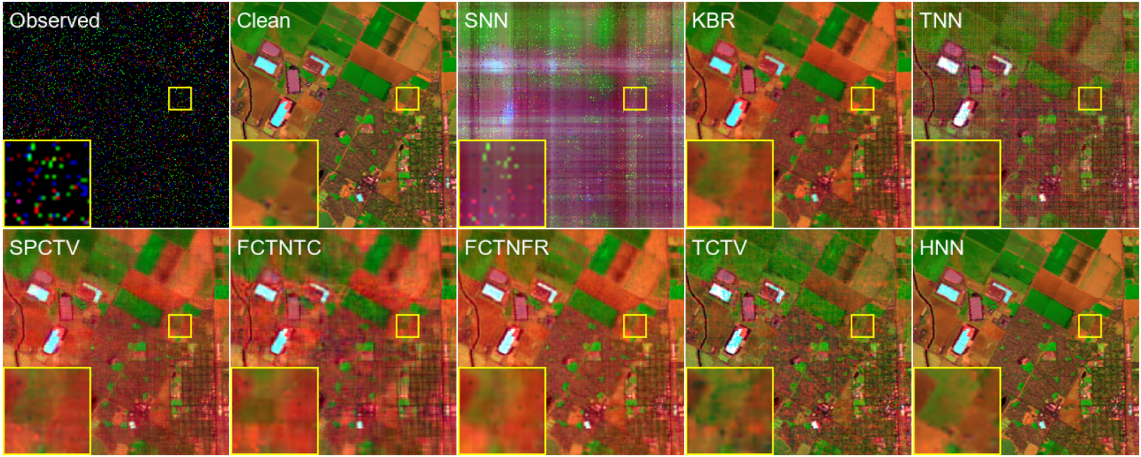


Fig. 4 False-color images (band: 193-97-19) of all compared methods on the BA dataset.

with factor regularization (FCTNFR) [47], and SPCTV [38], by varying the sampling rates (SR) at 4%, 5%, and 7%. Tables 3 and 4 present the performance metrics on the BA and PC datasets, respectively.

Table 3 shows that the HNN method outperforms other advanced methods in all evaluation metrics on the BA dataset. In terms of computational efficiency, the running times for the less effective KBR and TCTV methods are 1310.40s and 2020.76s, respectively, which are significantly higher than the HNN method’s running time of 177.13s. This indicates that the HNN method not only achieves best performance but also offers improved efficiency. As depicted in Table 4, the HNN approach consistently outperforms other methods on the PC dataset. For example, at a SR of 7%, it is evident that HNN shows a superior PSNR value compared to KBR and FCTBFR by 1.42 dB and 4.81 dB, respectively.

Fig. 4 depicts the false-color images on the BA dataset with a 5% SR. A notable observation is that the SNN method simply filled in the missing areas, while the TNN, SPCTV, FCTNTC, and FCTCFR methods introduced grid-like stripes. Only the KBR, TCTV, and HNN successfully restored the HSIs in a visually appealing manner. Among these, the HNN method stands out with its good results, for example, sharper textures and colors that closely resemble the original clear images. This confirms the effectiveness of the HNN method in the task of HSI inpainting.

6.4 Experiment on multi-temporal cloud removal

In this section, we concentrate on a specialized inpainting task: multi-temporal cloud removal. In this scenario, areas covered by clouds are considered missing pixels, and the objective is to reconstruct these pixels. However, clouds have distinctive shape patterns, making this task more challenging than randomly pixel missing cases.

A series of comprehensive synthetic experiments are conducted to evaluate the effectiveness of the HNN method. The synthetic datasets comprise two remote sensing images captured over Jizzakh by the Landsat-8 satellite, encompassing mountain and urban areas, with seven channels and nine time nodes. The size of these data is $512 \times 512 \times 7 \times 9$. To ensure the fidelity of the synthetic data to real-world conditions, we selected nine real cloud masks with varying levels of cloud coverage from the remote sensing cloud detection dataset.

Table 5 summarizes the performance metrics of all the compared methods on the Jizzakh mountain dataset. HNN demonstrates the most favorable performance. It consistently achieves the highest PSNR and SSIM scores while maintaining the lowest ERGAS and SAM scores across nearly all time nodes.

Table 6 presents the performance metrics on the Jizzakh urban dataset. As with the results obtained from the Jizzakh mountain dataset, it is evident that the HNN consistently achieves the best performance metrics across the majority of time nodes, with the second-best results observed at time nodes 1 and 9. In comparison to other methods, the results of HNN demonstrate both stability and superiority.

To further highlight the superiority of the HNN method, Fig. 5 displays false-color declouded images. To facilitate a detailed comparison, specific regions within each image are magnified for enhanced visibility. In Fig. 5, the SNN, SPCTV, and FCTNTC methods are observed to fill the cloud regions rather haphazardly, while the TNN and TCTV methods do not successfully reconstruct the original texture details beneath the clouds. The KBR and FCTNFR methods exhibit color discrepancies compared to the original images. Conversely, the HNN method effectively restores the intricate texture details, resulting in the restored images that closely resemble the original cloud-free images.

Table 5 Metrics on the Jizzakh mountain dataset. The best and the second best results are highlighted in **bold** and underline, respectively.

Time mode	Metrics	Obs	SNN	KBR	TNN	SPCTV	TNNTV	FCTNTC	FCTNFR	TCTV	HNN
#1	PSNR \uparrow	12.39	23.09	23.46	27.20	26.79	22.60	26.84	27.38	28.16	28.24
	SSIM \uparrow	0.5187	0.7961	0.8726	0.8875	0.8717	0.7746	0.8753	0.8916	0.9089	0.9323
	ERGAS \downarrow	764.33	182.84	173.29	113.07	117.77	191.43	117.39	110.69	<u>101.99</u>	100.84
	SAM \downarrow	0.6122	0.0751	0.0594	0.0593	0.0634	0.0673	0.0619	0.0603	<u>0.0554</u>	0.0343
#2	PSNR \uparrow	12.28	24.96	29.68	29.23	30.44	24.47	29.54	<u>32.09</u>	30.73	32.48
	SSIM \uparrow	0.5531	0.8299	0.9472	0.9141	0.9176	0.8009	0.9054	<u>0.9505</u>	0.9386	0.9659
	ERGAS \downarrow	801.33	152.17	89.77	92.49	80.35	160.63	88.65	<u>66.09</u>	78.44	64.46
	SAM \downarrow	0.5067	0.0420	<u>0.0213</u>	0.0332	0.0406	0.0403	0.0335	0.0245	0.0294	0.0156
#3	PSNR \uparrow	14.01	27.60	33.81	32.49	33.40	27.26	32.22	<u>35.21</u>	34.13	36.23
	SSIM \uparrow	0.6819	0.9017	<u>0.9749</u>	0.9511	0.9534	0.8892	0.9418	0.9739	0.9675	0.9859
	ERGAS \downarrow	594.71	110.81	<u>55.57</u>	63.09	56.60	114.86	64.70	46.07	52.40	41.85
	SAM \downarrow	0.3363	0.0265	0.0114	0.0207	0.0215	0.0231	0.0255	<u>0.0167</u>	0.0180	0.0080
#4	PSNR \uparrow	13.24	26.34	31.83	30.02	32.01	25.64	30.83	33.28	31.81	34.24
	SSIM \uparrow	0.7193	0.8857	<u>0.9726</u>	0.9374	0.9506	0.8613	0.9369	0.9697	0.9571	0.9802
	ERGAS \downarrow	663.22	128.05	68.36	82.72	65.55	138.33	75.18	56.89	67.37	61.29
	SAM \downarrow	0.3519	0.0245	0.0095	0.0206	0.0158	0.0240	0.0190	0.0137	0.0179	0.0082
#5	PSNR \uparrow	10.54	23.02	27.59	28.58	30.26	23.85	29.28	31.72	29.42	32.59
	SSIM \uparrow	0.4817	0.7669	0.9340	0.8807	0.8992	0.7331	0.8765	<u>0.9386</u>	0.9146	0.9610
	ERGAS \downarrow	1052.98	185.63	108.97	95.38	78.63	165.94	87.76	<u>66.56</u>	87.25	61.15
	SAM \downarrow	0.6842	0.0475	<u>0.0238</u>	0.0386	0.0297	0.0448	0.0346	0.0259	0.0370	0.0159
#6	PSNR \uparrow	12.39	24.03	24.99	28.15	31.16	23.45	30.42	31.95	27.90	32.80
	SSIM \uparrow	0.6147	0.8421	0.9229	0.9025	0.9247	0.8154	0.9120	<u>0.9415</u>	0.9153	0.9660
	ERGAS \downarrow	699.76	159.04	140.87	98.41	68.07	169.59	74.07	<u>62.35</u>	100.54	58.96
	SAM \downarrow	0.4981	0.0535	0.0362	0.0438	0.0312	0.0551	0.0343	<u>0.0279</u>	0.0385	0.0187
#7	PSNR \uparrow	20.65	31.62	31.33	32.98	32.83	31.61	32.18	30.86	33.82	<u>33.21</u>
	SSIM \uparrow	0.9162	0.9647	0.9709	0.9733	0.9655	0.9638	0.9646	0.9632	0.9774	<u>0.9756</u>
	ERGAS \downarrow	248.40	68.02	73.98	59.48	60.15	68.41	63.95	75.15	54.14	<u>57.84</u>
	SAM \downarrow	0.0956	0.0095	0.0098	0.0099	0.0121	<u>0.0082</u>	0.0122	0.0125	0.0092	0.0081
#8	PSNR \uparrow	14.17	25.66	26.79	29.07	<u>29.97</u>	25.19	29.29	29.93	29.94	31.07
	SSIM \uparrow	0.7535	0.8883	0.9289	0.9320	0.9268	0.8765	0.9247	0.9411	<u>0.9437</u>	0.9613
	ERGAS \downarrow	541.15	130.14	119.73	89.92	79.98	137.46	85.99	80.78	82.59	71.08
	SAM \downarrow	0.2950	0.0352	0.0296	0.0304	0.0563	0.0311	0.0370	0.0377	0.0299	0.0199
#9	PSNR \uparrow	14.61	26.19	27.66	29.64	30.50	25.47	29.79	30.08	30.91	31.47
	SSIM \uparrow	0.7734	0.9105	0.9439	0.9426	0.9369	0.9024	0.9353	0.9488	<u>0.9560</u>	0.9664
	ERGAS \downarrow	514.77	124.67	108.15	83.85	75.66	135.52	81.86	79.63	72.40	68.25
	SAM \downarrow	0.2575	0.0261	<u>0.0201</u>	0.0227	0.0363	0.0236	0.0287	0.0290	0.0218	0.0140
Mean	PSNR \uparrow	13.81	25.83	28.57	29.71	30.82	25.51	30.04	31.39	30.76	32.48
	SSIM \uparrow	0.6681	0.8651	0.9409	0.9246	0.9274	0.8463	0.9192	<u>0.9465</u>	0.9421	0.9661
	ERGAS \downarrow	686.20	142.25	110.09	87.94	77.73	146.45	83.56	<u>73.64</u>	79.27	65.81
	SAM \downarrow	0.5160	0.1333	0.1047	0.0853	0.0766	0.1300	0.0787	<u>0.0684</u>	0.0766	0.0550

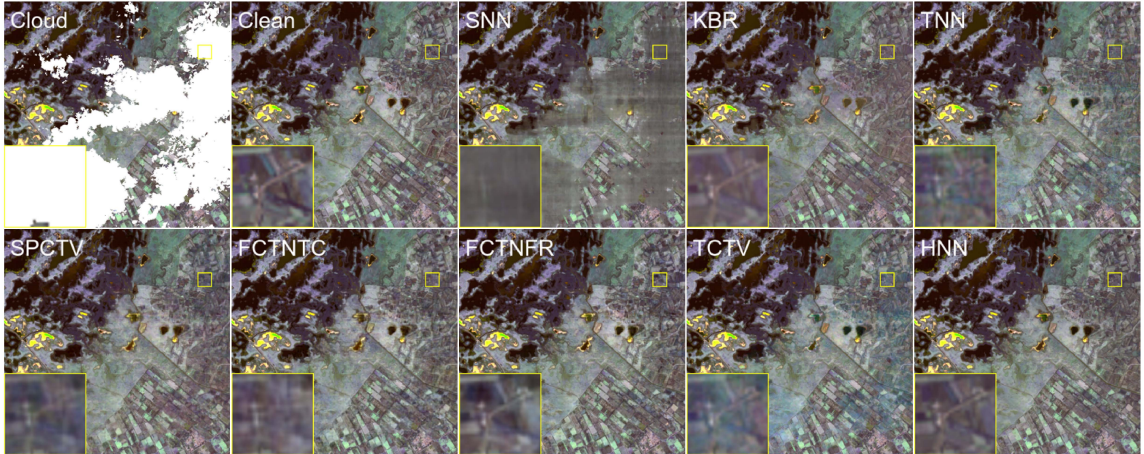


Fig. 5 The false-color decloud images (the 5th time node, band 1-4-7) of all compared methods on the Jizzakh mountain dataset.

6.5 Discussion

6.5.1 Running time

Table 7 compares the execution times of all methods. For inpainting, HNN is notably faster than FCTNFR and TCTV. SNN is the only method

faster than HNN, but SNN does not yield satisfactory restoration results. Fig. 6 presents a scatter plot of the Jizzakh mountain dataset, clearly illustrating the performance-time relationship. Remarkably, HNN achieves the highest PSNR while maintaining relatively short execution times. In contrast, although TCTV and FCTNFR yield impressive

Table 6 Metrics on the Jizzakh urban dataset. The best and the second best results are highlighted in **bold** and underline, respectively.

Time mode	Metrics	Obs	SNN	KBR	TNN	SPCTV	TNNTV	FCTNTC	FCTNFR	TCTV	HNN
#1	PSNR↑	10.71	24.92	26.41	24.69	25.16	25.03	24.84	24.50	25.32	<u>26.30</u>
	SSIM↑	0.4982	0.7665	<u>0.8487</u>	0.7846	0.7877	0.7506	0.7880	0.8070	0.8174	0.8515
	ERGAS↓	892.96	137.10	114.27	140.64	131.42	135.40	136.45	141.58	131.03	<u>116.67</u>
	SAM↓	0.6135	0.0403	<u>0.0365</u>	0.0457	0.0400	0.0401	0.0441	0.0449	0.0417	0.0311
#2	PSNR↑	12.31	24.39	26.89	25.56	27.43	24.38	26.95	<u>27.73</u>	27.15	28.76
	SSIM↑	0.5487	0.8036	<u>0.9062</u>	0.8408	0.8737	0.7844	0.8650	0.8985	0.8806	0.9279
	ERGAS↓	753.35	156.03	115.24	134.02	108.08	156.19	114.02	<u>104.07</u>	112.21	93.24
	SAM↓	0.5071	0.0463	0.0356	0.0475	0.0315	0.0463	0.0353	<u>0.0308</u>	0.0410	0.0215
#3	PSNR↑	14.08	26.91	30.99	28.56	30.90	26.89	30.43	<u>31.47</u>	30.86	32.88
	SSIM↑	0.6720	0.8837	<u>0.9589</u>	0.9109	0.9322	0.8686	0.9234	0.9474	0.9387	0.9680
	ERGAS↓	566.35	115.47	71.75	94.38	71.86	116.48	75.89	<u>67.32</u>	73.07	57.39
	SAM↓	0.3369	0.0265	<u>0.0162</u>	0.0271	0.0180	0.0264	0.0203	0.0178	0.0224	0.0109
#4	PSNR↑	14.11	26.79	29.53	27.63	30.22	26.59	29.79	<u>30.64</u>	29.80	32.63
	SSIM↑	0.7192	0.8707	<u>0.9498</u>	0.8906	0.9242	0.8561	0.9192	0.9426	0.9241	0.9652
	ERGAS↓	559.53	115.78	85.12	104.00	77.00	119.17	80.97	<u>73.42</u>	81.27	58.71
	SAM↓	0.3519	0.0283	0.0217	0.0304	0.0193	0.0282	0.0217	<u>0.0192</u>	0.0256	0.0128
#5	PSNR↑	10.51	23.69	28.00	25.48	28.28	23.86	27.83	<u>28.72</u>	26.87	29.91
	SSIM↑	0.4747	0.7441	<u>0.9092</u>	0.8088	0.8617	0.7160	0.8485	0.8976	0.8619	0.9339
	ERGAS↓	965.49	163.06	97.45	130.22	94.18	159.82	98.63	<u>89.64</u>	110.73	79.05
	SAM↓	0.6844	0.0439	0.0303	0.0494	<u>0.0299</u>	0.0458	0.0340	0.0311	0.0456	0.0201
#6	PSNR↑	11.22	25.84	<u>29.78</u>	24.83	29.17	25.75	28.52	28.32	25.17	30.64
	SSIM↑	0.6041	0.8245	<u>0.9271</u>	0.8323	0.8877	0.8073	0.8747	0.8961	0.8562	0.9378
	ERGAS↓	772.65	120.82	<u>77.19</u>	137.24	81.76	121.98	88.08	90.01	133.95	69.32
	SAM↓	0.4985	0.0246	<u>0.0148</u>	0.0394	0.0197	0.0267	0.0240	0.0242	0.0378	0.0142
#7	PSNR↑	18.74	30.30	<u>32.69</u>	29.02	31.97	30.19	30.21	29.98	29.64	33.05
	SSIM↑	0.9108	0.9581	0.9723	0.9502	0.9631	0.9595	0.9573	0.9588	0.9568	<u>0.9721</u>
	ERGAS↓	292.35	78.54	<u>60.25</u>	90.79	64.51	79.57	79.13	80.73	84.09	57.42
	SAM↓	0.0958	0.0114	0.0083	0.0128	<u>0.0083</u>	0.0111	0.0104	0.0100	0.0117	0.0073
#8	PSNR↑	13.42	26.36	<u>28.07</u>	25.59	27.53	26.45	26.74	26.69	26.26	28.11
	SSIM↑	0.7359	0.8743	<u>0.9181</u>	0.8768	0.8935	0.8674	0.8883	0.9040	0.8933	0.9203
	ERGAS↓	553.45	114.75	92.56	126.79	98.76	114.00	108.27	108.49	118.66	<u>92.74</u>
	SAM↓	0.2967	0.0211	<u>0.0162</u>	0.0257	0.0186	0.0213	0.0211	0.0217	0.0245	0.0155
#9	PSNR↑	14.50	26.48	28.45	26.67	27.83	26.56	26.82	26.68	27.82	<u>28.21</u>
	SSIM↑	0.7625	0.8965	0.9333	0.9028	0.9109	0.8921	0.9055	0.9173	0.9218	<u>0.9329</u>
	ERGAS↓	502.23	117.70	92.13	114.61	99.04	117.36	111.52	113.68	100.09	<u>95.54</u>
	SAM↓	0.2585	0.0213	<u>0.0163</u>	0.0235	0.0176	0.0213	0.0204	0.0217	0.0211	0.0145
Mean	PSNR↑	13.29	26.19	<u>28.98</u>	26.45	28.72	26.19	28.02	28.30	27.65	30.05
	SSIM↑	0.6584	0.8469	<u>0.9248</u>	0.8664	0.8927	0.8335	0.8855	0.9077	0.8945	0.9344
	ERGAS↓	680.84	126.60	<u>91.21</u>	120.51	93.88	126.50	101.02	98.96	107.02	82.41
	SAM↓	0.5059	0.0861	<u>0.0641</u>	0.0884	0.0673	0.0871	0.0722	0.0702	0.0791	0.0537

results, their lengthy execution times are a concern. Similarly, while SNN and TNN have shorter execution times, their PSNR does not meet expectations.

6.5.2 Numerical Analysis of Convergence

The algorithm’s convergence is guaranteed by the fact that the current model satisfies the sufficient conditions for ADMM convergence. To further validate its convergence, we conduct a numerical analysis of the HNN’s convergence. Fig. 7 depicts the curves of PSNR, SSIM, ERGAS, and SAM values versus the number of iterations on the Jizzakh mountain dataset. Notably, after 40 iterations, their values reach a stable state. This observation

provides further evidence for the convergence of the ADMM algorithm employed in this study for solving the HNN model.

6.5.3 Influence of the Temporal Number

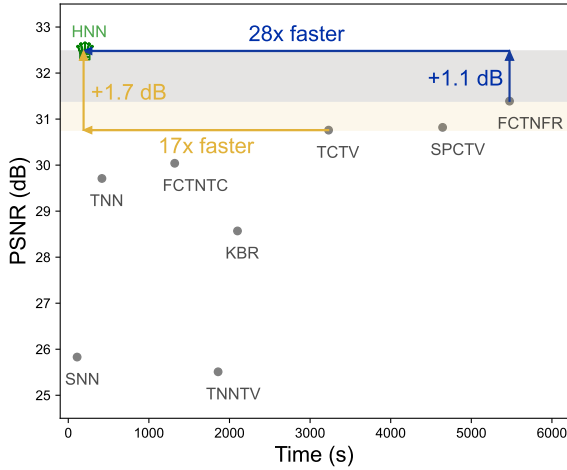
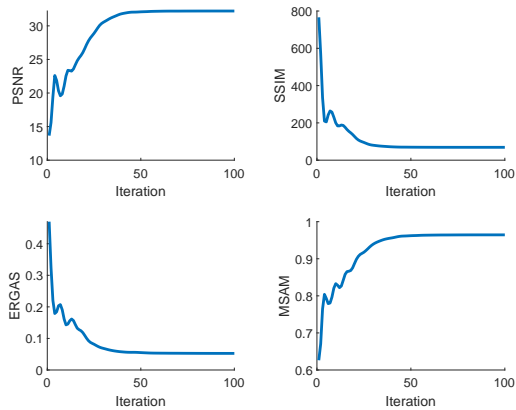
This section explores the influence of temporal number on HNN’s performance, by varying the temporal number on the Jizzakh mountain dataset. Recalling the results with 9 time nodes (listed in Table 5), it is shown that, if not considering HNN, FCTNFC and TCTV are two best performer among the existing methods, achieving PSNR values of 31.39 dB and 30.76 dB, respectively. However, Table 8 shows that the HNN achieves PSNR values of 31.80 dB with only 6 time nodes, surpassing the

Table 7 The running time of compared methods (in seconds).

Task	Datasets	SNN	KBR	TNN	SPCTV	TNNTV	FCTNTC	FCTNFR	TCTV	HNN
HSI Inpainting	BA	71.19	1310.4	219.42	3272.72	1108.82	244.23	285.69	2020.76	<u>177.13</u>
	PC	18.45	276.63	39.38	885.58	211.36	68.22	101.13	275.12	60.13
Cloud Removal	Mountain	109.54	2099.33	417.33	4643.82	1858.6	1320.26	5474.12	3229.33	<u>190.36</u>
	Urban	71.71	1730.17	348.06	3953.04	1828.23	968.53	4682.67	3105.27	<u>183.75</u>
	Real-world	89.33	727.18	139.41	1445.49	501.31	373.3	1317.16	891.96	43.71
Task	Datasets	LLRT	TDL	LTDL	NGMeet	CTV	3DTNN	3DLogTNN	WNLRTV	HNN
HSI Denoising	BA	1456.47	32.73	16160.75	<u>75.23</u>	118.97	259.68	387.73	646.28	84.85
	PC	399.67	6.8	15060.76	35.03	21.48	46.25	70.40	200.43	<u>19.53</u>

Table 8 Metrics on the Jizzakh mountain dataset with varying temporal numbers.

Metrics	3	4	5	6	7	8	9
PSNR	24.33	28.86	30.58	31.80	32.21	32.09	32.48
SSIM	0.9142	0.9488	0.9527	0.9609	0.9645	0.9619	0.9661
ERGAS	161.97	98.36	84.04	73.06	68.93	71.31	65.81
SAM	0.0847	0.0606	0.0551	0.0539	0.0526	0.0578	0.0550

**Fig. 6** The scatter plot of PSNR versus time for the Jizzakh mountain dataset.**Fig. 7** Metric curves versus iteration number.

performance of the existing methods by a considerable improvement. This result further confirms the effectiveness of the HNN method.

7 Conclusion

This paper introduces the HNN as a regularization term for remote sensing image restoration. HNN effectively combines low-rank and smoothness priors and is computationally efficient. Its superior performance in inpainting, denoising, and cloud removal tasks makes it a valuable tool for enhancing the quality and utility of remote sensing imagery. Future research can explore the application of HNN in other remote sensing image processing tasks, such as HSI unmixing and classification.

References

- [1] Yi Chang, Luxin Yan, and Sheng Zhong. Hyper-laplacian regularized unidirectional low-rank tensor recovery for multispectral image denoising. In *2017 IEEE Conference on Computer Vision and Pattern Recognition, CVPR 2017, Honolulu, HI, USA, July 21-26, 2017*, pages 5901–5909. IEEE Computer Society, 2017.
- [2] Yang Chen, Wenfei Cao, Li Pang, and Xiangyong Cao. Hyperspectral image denoising with weighted nonlocal low-rank model and adaptive total variation regularization. *IEEE Trans. Geosci. Remote. Sens.*, 60:1–15, 2022.
- [3] Yang Chen, Xiangyong Cao, Qian Zhao, Deyu Meng, and Zongben Xu. Denoising hyperspectral image with non-i.i.d. noise structure. *IEEE Trans. Cybern.*, 48(3):1054–1066, 2018.
- [4] Yong Chen, Wei He, Naoto Yokoya, Ting-Zhu Huang, and Xi-Le Zhao. Nonlocal tensor-ring decomposition for hyperspectral image denoising. *IEEE Trans. Geosci. Remote. Sens.*, 58(2):1348–1362, 2020.
- [5] Yong Chen, Ting-Zhu Huang, Wei He, Xi-Le Zhao, Hongyan Zhang, and Jinshan Zeng. Hyperspectral image denoising using factor group sparsity-regularized nonconvex low-rank approximation. *IEEE Trans. Geosci. Remote.*

- Sens.*, 60:1–16, 2022.
- [6] Yongyong Chen, Yanwen Guo, Yongli Wang, Dong Wang, Chong Peng, and Guoping He. Denoising of hyperspectral images using non-convex low rank matrix approximation. *IEEE Trans. Geosci. Remote. Sens.*, 55(9):5366–5380, 2017.
- [7] Lieven De Lathauwer, Bart De Moor, and Joos Vandewalle. A multilinear singular value decomposition. *SIAM Journal on Matrix Analysis and Applications*, 21(4):1253–1278, 2000.
- [8] Silvia Gandy, Benjamin Recht, and Isao Yamada. Tensor completion and low-n-rank tensor recovery via convex optimization. *Inverse Problems*, 27(2):025010, jan 2011.
- [9] Wei He, Quanming Yao, Chao Li, Naoto Yokoya, Qibin Zhao, Hongyan Zhang, and Liangpei Zhang. Non-local meets global: An iterative paradigm for hyperspectral image restoration. *IEEE Trans. Pattern Anal. Mach. Intell.*, 44(4):2089–2107, 2022.
- [10] Wei He, Hongyan Zhang, Liangpei Zhang, and Huanfeng Shen. Total-variation-regularized low-rank matrix factorization for hyperspectral image restoration. *IEEE Trans. Geosci. Remote. Sens.*, 54(1):178–188, 2016.
- [11] F. L. Hitchcock. The expression of a tensor or a polyadic as a sum of products. *J. Math. Phys.*, 6(1-4):164–189, 1927.
- [12] Danfeng Hong, Wei He, Naoto Yokoya, Jing Yao, Lianru Gao, Liangpei Zhang, Jocelyn Chanussot, and Xiaoxiang Zhu. Interpretable hyperspectral artificial intelligence: When non-convex modeling meets hyperspectral remote sensing. *IEEE Geoscience and Remote Sensing Magazine*, 9(2):52–87, 2021.
- [13] Xingfang Huang, Shuang Xu, Chunxia Zhang, and Jiangshe Zhang. Robust CP tensor factorization with skew noise. *IEEE Signal Process. Lett.*, 27:785–789, 2020.
- [14] M. E. Kilmer, K. Braman, N. Hao, and R. C. Hoover. Third-order tensors as operators on matrices: A theoretical and computational framework with applications in imaging. *SIAM J. Matrix Anal. Appl.*, 34(1):148–172, 2013.
- [15] Ching-Yun Ko, Kim Batselier, Luca Daniel, Wenjian Yu, and Ngai Wong. Fast and accurate tensor completion with total variation regularized tensor trains. *IEEE Trans. Image Process.*, 29:6918–6931, 2020.
- [16] Xutao Li, Yunming Ye, and Xiaofei Xu. Low-rank tensor completion with total variation for visual data inpainting. In Satinder Singh and Shaul Markovitch, editors, *Proceedings of the Thirty-First AAAI Conference on Artificial Intelligence, February 4-9, 2017, San Francisco, California, USA*, pages 2210–2216. AAAI Press, 2017.
- [17] Ji Liu, Przemyslaw Musialski, Peter Wonka, and Jieping Ye. Tensor completion for estimating missing values in visual data. *IEEE Trans. Pattern Anal. Mach. Intell.*, 35(1):208–220, 2013.
- [18] Zhen Long, Ce Zhu, Jiani Liu, and Yipeng Liu. Bayesian low rank tensor ring for image recovery. *IEEE Trans. Image Process.*, 30:3568–3580, 2021.
- [19] Canyi Lu, Jiashi Feng, Zhouchen Lin, and Shuicheng Yan. Exact low tubal rank tensor recovery from gaussian measurements. In Jérôme Lang, editor, *International Joint Conference on Artificial Intelligence, IJCAI, July 13-19, 2018, Stockholm, Sweden*, pages 2504–2510, 2018.
- [20] Canyi Lu, Xi Peng, and Yunchao Wei. Low-rank tensor completion with a new tensor nuclear norm induced by invertible linear transforms. In *Computer Vision and Pattern Recognition, CVPR, Long Beach, CA, USA, June 16-20, 2019*, pages 5996–6004, 2019.
- [21] I. V. Oseledets. Tensor-train decomposition. *SIAM J. Sci. Comput.*, 33(5):2295–2317, 2011.
- [22] Chong Peng, Yang Liu, Kehan Kang, Yongyong Chen, Xinxing Wu, Andrew Cheng, Zhao Kang, Chenglizhao Chen, and Qiang Cheng. Hyperspectral image denoising using nonconvex local low-rank and sparse separation with spatial-spectral total variation regularization. *IEEE Trans. Geosci. Remote. Sens.*, 60:1–17, 2022.
- [23] Jiangjun Peng, Hailin Wang, Xiangyong Cao, Qian Zhao, Jing Yao, Hongying Zhang, and Deyu Meng. Learnable representative coefficient image denoiser for hyperspectral image. *IEEE Trans. Geosci. Remote. Sens.*, 62:1–16, 2024.
- [24] Jiangjun Peng, Yao Wang, Hong-Ying Zhang, Jianjun Wang, and Deyu Meng. Exact decomposition of joint low rankness and local smoothness plus sparse matrices. *IEEE Trans. Pattern Anal. Mach. Intell.*, 45(5):5766–5781, 2023.
- [25] Jiangjun Peng, Qi Xie, Qian Zhao, Yao Wang, Yee Leung, and Deyu Meng. Enhanced 3dtv regularization and its applications on HSI denoising and compressed sensing. *IEEE Trans. Image Process.*, 29:7889–7903, 2020.
- [26] Yi Peng, Deyu Meng, Zongben Xu, Chenqiang Gao, Yi Yang, and Biao Zhang. Decomposable nonlocal tensor dictionary learning for multispectral image denoising. In *2014 IEEE Conference on Computer Vision and Pattern Recognition, CVPR 2014, Columbus, OH, USA, June 23-28, 2014*, pages 2949–2956. IEEE Computer Society, 2014.
- [27] Duo Qiu, Minru Bai, Michael K. Ng, and Xiongjun Zhang. Robust low-rank tensor completion via transformed tensor nuclear norm

- with total variation regularization. *Neurocomputing*, 435:197–215, 2021.
- [28] Yuning Qiu, Guoxu Zhou, Qibin Zhao, and Shengli Xie. Noisy tensor completion via low-rank tensor ring. *IEEE Trans. Neural Networks Learn. Syst.*, 35(1):1127–1141, 2024.
- [29] L. R. Tucker. Implications of factor analysis of three-way matrices for measurement of change. *Probl. Meas. Change*, 15:122–137, May 1963.
- [30] Hailin Wang, Jiangjun Peng, Xiangyong Cao, Jianjun Wang, Qibin Zhao, and Deyu Meng. Hyperspectral image denoising via nonlocal spectral sparse subspace representation. *IEEE J. Sel. Top. Appl. Earth Obs. Remote. Sens.*, 16:5189–5203, 2023.
- [31] Hailin Wang, Jiangjun Peng, Wenjin Qin, Jianjun Wang, and Deyu Meng. Guaranteed tensor recovery fused low-rankness and smoothness. *IEEE Trans. Pattern Anal. Mach. Intell.*, 45(9):10990–11007, 2023.
- [32] Yao Wang, Jiangjun Peng, Qian Zhao, Yee Leung, Xi-Le Zhao, and Deyu Meng. Hyperspectral image restoration via total variation regularized low-rank tensor decomposition. *IEEE J. Sel. Top. Appl. Earth Obs. Remote. Sens.*, 11(4):1227–1243, 2018.
- [33] Qi Xie, Qian Zhao, Deyu Meng, and Zongben Xu. Kronecker-basis-representation based tensor sparsity and its applications to tensor recovery. *IEEE Trans. Pattern Anal. Mach. Intell.*, 40(8):1888–1902, 2018.
- [34] Shuang Xu, Xiangyong Cao, Jiangjun Peng, Qiao Ke, Cong Ma, and Deyu Meng. Hyperspectral image denoising by asymmetric noise modeling. *IEEE Trans. Geosci. Remote. Sens.*, 60:1–14, 2022.
- [35] Shuang Xu, Chunxia Zhang, and Jianshe Zhang. Adaptive quantile low-rank matrix factorization. *Pattern Recognit.*, 103:107310, 2020.
- [36] Jize Xue, Yongqiang Zhao, Wenzhi Liao, and Jonathan Cheung-Wai Chan. Nonconvex tensor rank minimization and its applications to tensor recovery. *Inf. Sci.*, 503:109–128, 2019.
- [37] Jize Xue, Yongqiang Zhao, Wenzhi Liao, and Jonathan Cheung-Wai Chan. Nonlocal low-rank regularized tensor decomposition for hyperspectral image denoising. *IEEE Trans. Geosci. Remote. Sens.*, 57(7):5174–5189, 2019.
- [38] Tatsuya Yokota, Qibin Zhao, and Andrzej Cichocki. Smooth PARAFAC decomposition for tensor completion. *IEEE Trans. Signal Process.*, 64(20):5423–5436, 2016.
- [39] Qiang Zhang, Yaming Zheng, Qiangqiang Yuan, Meiping Song, Haoyang Yu, and Yi Xiao. Hyperspectral image denoising: From model-driven, data-driven, to model-data-driven. *IEEE Transactions on Neural Networks and Learning Systems*, in press:1–21, 2023.
- [40] Qibin Zhao, Guoxu Zhou, Shengli Xie, Liqing Zhang, and Andrzej Cichocki. Tensor ring decomposition. *CoRR*, abs/1606.05535, 2016.
- [41] Wen-Jie Zheng, Xi-Le Zhao, Yu-Bang Zheng, and Ting-Zhu Huang. Provable stochastic algorithm for large-scale fully-connected tensor network decomposition. *Journal of Scientific Computing*, 98(1):1–16, 2024.
- [42] Wen-Jie Zheng, Xi-Le Zhao, Yu-Bang Zheng, Jie Lin, Lina Zhuang, and Ting-Zhu Huang. Spatial-spectral-temporal connective tensor network decomposition for thick cloud removal. *ISPRS Journal of Photogrammetry and Remote Sensing*, 199:182–194, 2023.
- [43] Wen-Jie Zheng, Xi-Le Zhao, Yu-Bang Zheng, and Zhi-Feng Pang. Nonlocal patch-based fully connected tensor network decomposition for multispectral image inpainting. *IEEE Geoscience and Remote Sensing Letters*, 19:1–5, art no. 8025105, 2022.
- [44] Yu-Bang Zheng, Ting-Zhu Huang, Xi-Le Zhao, Yong Chen, and Wei He. Double-factor-regularized low-rank tensor factorization for mixed noise removal in hyperspectral image. *IEEE Transactions on Geoscience and Remote Sensing*, 58(12):8450–8464, 2020.
- [45] Yu-Bang Zheng, Ting-Zhu Huang, Xi-Le Zhao, Tai-Xiang Jiang, Teng-Yu Ji, and Tian-Hui Ma. Tensor N-tubal rank and its convex relaxation for low-rank tensor recovery. *Information Sciences*, 532:170–189, 2020.
- [46] Yu-Bang Zheng, Ting-Zhu Huang, Xi-Le Zhao, Tai-Xiang Jiang, Tian-Hui Ma, and Teng-Yu Ji. Mixed noise removal in hyperspectral image via low-fibered-rank regularization. *IEEE Transactions on Geoscience and Remote Sensing*, 58(1):734–749, 2020.
- [47] Yu-Bang Zheng, Ting-Zhu Huang, Xi-Le Zhao, and Qibin Zhao. Tensor completion via fully-connected tensor network decomposition with regularized factors. *Journal of Scientific Computing*, 92:1–35, 2022.
- [48] Yu-Bang Zheng, Ting-Zhu Huang, Xi-Le Zhao, Qibin Zhao, and Tai-Xiang Jiang. Fully-connected tensor network decomposition and its application to higher-order tensor completion. In *Thirty-Fifth AAAI Conference on Artificial Intelligence Virtual Event, February 2-9*, pages 11071–11078, 2021.
- [49] Yu-Bang Zheng, Xi-Le Zhao, Junhua Zeng, Chao Li, Qibin Zhao, Heng-Chao Li, and Ting-Zhu Huang. Svdinstn: A tensor network paradigm for efficient structure search from regularized modeling perspective. In *2024 IEEE/CVF Conference on Computer Vision and Pattern Recognition (CVPR)*, 2024.
- [50] Lina Zhuang and Michael K. Ng. Hyperspectral mixed noise removal by ℓ_1 -norm-based subspace representation. *IEEE J. Sel. Top.*

Appl. Earth Obs. Remote. Sens., 13:1143–
1157, 2020.